

Microseismicity and lithosphere thickness at a nearly-amagmatic oceanic detachment fault system

Received: 1 December 2021

Jie Chen¹✉, Wayne C. Crawford¹ & Mathilde Cannat¹

Accepted: 16 January 2023

Published online: 26 January 2023

 Check for updates

Oceanic detachment faults play a central role in accommodating the plate divergence at slow-ultraslow spreading mid-ocean ridges. Successive flip-flop detachment faults in a nearly-amagmatic region of the ultraslow spreading Southwest Indian Ridge (SWIR) at 64°30'E accommodate ~100% of plate divergence, with mostly ultramafic smooth seafloor. Here we present microseismicity data, recorded by ocean bottom seismometers, showing that the axial brittle lithosphere is on the order of 15 km thick under the nearly-amagmatic smooth seafloor, which is no thicker than under nearby volcanic seafloor or at more magmatic SWIR detachment systems. Our data reveal that microearthquakes with normal focal mechanisms are colocated with seismically-imaged damage zones of the active detachment fault and of antithetic hanging-wall faults. The level of the hanging-wall seismicity is significantly higher than that documented at more magmatic detachments of slow-ultraslow ridges, which may be a unique feature of nearly-amagmatic flip-flop detachment systems.

The flip-flop detachment fault system discovered at a nearly amagmatic region of the ultraslow spreading Southwest Indian Ridge (SWIR; full spreading rate of 14 mm/yr) near 64°30'E represents a previously unknown seafloor spreading mode^{1–3} (Fig. 1a). In this mode, detachment faults accommodate nearly 100% of plate divergence, continuously cutting into the footwalls of their predecessors, with flipping polarities every 0.6–1.5 Ma¹² (Fig. 1). The resulting seafloor morphology is the so-called smooth seafloor⁴, with extensive exposure of mantle-derived peridotites, only patches of hummocky basalts², and low-temperature carbonate-brucite hydrothermal chimneys⁵. This newly discovered seafloor spreading mode differs from the “classic” detachment–volcanic and volcanic–volcanic modes at slow spreading ridges and at more magmatically robust portions of ultraslow spreading ridges, where at least one plate is dominated by abyssal-hill volcanic seafloor^{4,6–9} and the detachment fault is characterized by dome-shaped corrugated surface^{10–12}.

Seismicity provides a means to study magmatic, tectonic, and hydrothermal processes within the lithosphere of mid-ocean ridges^{13–19} (MORs) and is an indirect proxy for the thermal regime by constraining the depth to the base of the brittle lithosphere^{20,21}. Here, we present a

catalog of 307 microearthquakes recorded during two short (8 and 19 days for the SMSMO and RVS MO catalogs, respectively) ocean bottom seismometer (OBS) deployments (Figs. 1, 2a; see the “Methods” section). These microearthquakes and 8 focal mechanisms (see the “Methods” section) reveal a unique distribution of geodynamic stress and accommodation at the youngest active detachment system (DF1) of the SWIR 64°30'E.

Results and discussion

Microseismicity at the SWIR 64°30'E

The two short OBS deployments offer snapshots in time of the seismic activity at the youngest active detachment system. The average seismicity rate is 11.4 events per day (8.4 and 12.7 events per day in the SMSMO and RVS MO catalogs, respectively), including a 34-event seismic swarm in the RVS MO catalog, during December 22–23, 2016 (Supplementary Fig. 5). Most microearthquakes occurred in the axial valley (Fig. 2a) between the emergence of DF1 (E1) and the breakaway of DF2 (B2). The highest number of events is recorded near the P2–P2' cross-axis profile (Fig. 2a, c). Earthquake hypocenters have depths between 0 and 15 km below the seafloor (bsf), and events in the shorter

¹Université Paris Cité, Institut de physique du globe de Paris, CNRS, F-75005 Paris, France. ✉ e-mail: chenjie.geo@outlook.com

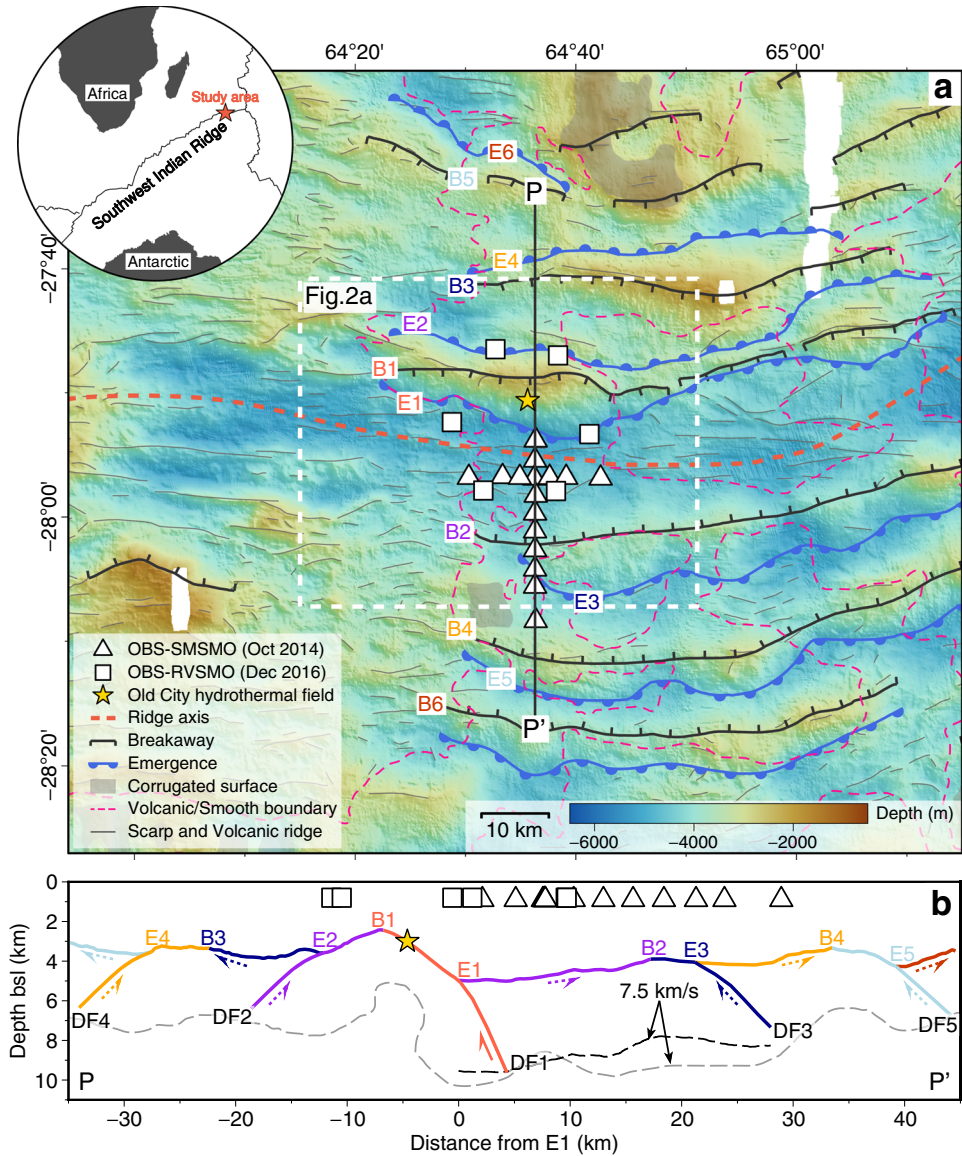


Fig. 1 | OBS locations and tectonic interpretation of the flip-flop detachment fault system at the eastern SWIR. **a** Tectonic map with locations of the OBS networks: SMSMO (14 OBSs) and RVSOMO (6 OBSs). The base map is created based on shipborne bathymetry data⁴. Geological and tectonic information (see legend for symbols) includes breakaways (B1–B6) and emergences (E1–E6) of successive detachment faults, corrugated surface, the boundary between volcanic and smooth seafloor, and linear sketches of scarps and volcanic ridges⁵. Yellow star is the low-

temperature Old City hydrothermal field with carbonate-brucite chimneys⁵. The white dashed square marks the bounds of Fig. 2a. **b** Tectonic interpretation of the successive flip-flop detachment fault system along the PP' cross-section¹. Black and gray dashed lines are the 7.5 km/s velocity contours constrained by seismic tomography^{23,39}. Locations of OBSs are projected to the PP' cross-section. bsl below sea level, SWIR Southwest Indian Ridge, DF detachment fault, OBS ocean-bottom seismometer, SMSMO SISMOSMOOTH cruise, RVSOMO ROVSMOOTH cruise.

SMSMO catalog were mostly at <10 km bsf (Fig. 2b). Local magnitudes (M_L) range from −0.5 to 3.2, with a magnitude of completeness of 1.1 and a b -value of 0.9 based on the Gutenberg–Richter relation²² (see the “Methods” section and Supplementary Fig. 6). Focal mechanisms (see the “Methods” section) correspond to normal faulting, as expected in an extensional context, except for one strike-slip faulting event (Fig. 2a).

Many microearthquake hypocenters plotted in the cross-axis profiles P1–P1' and P2–P2' (Fig. 2d, e) are aligned with the trace of the subseafloor detachment fault plane as inferred from a series of subparallel seismic reflectors with a dip of 50–60°^{23,24}. In all three cross-axis profiles, and particularly P3–P3', several events are scattered in the detachment hanging wall. Focal mechanisms of these hanging-wall earthquakes display a prevalence of normal faults with an average dip of 50° at 2–7 km bsf (Fig. 2e, f). These dips are consistent with the

geometry of nearby north-dipping seismic reflectors²³ (Fig. 2f) and with small-offset fault scarps at the seafloor², suggesting that these small faults are conjugate with the detachment fault.

Along the ridge axis (P0–P0'), we also observed a larger number of earthquakes at the transition between volcanic and smooth seafloor (near the P2–P2' profile; Fig. 2c, e). Combining this observation with the previous observation of subhorizontal seismic reflectors interpreted as intrusive magmatic sills beneath this transition²⁴, we propose that seismicity may be elevated here because the crystallized basalts or gabbros (beneath the volcanic seafloor) are more prone to seismogenic rupture than the ultramafic basement (beneath the smooth seafloor) in which stress may be accommodated by creep due to serpentization. Our observations may thus provide a framework to examine earthquake generation at detachment systems, interacting with sparse magmatism.

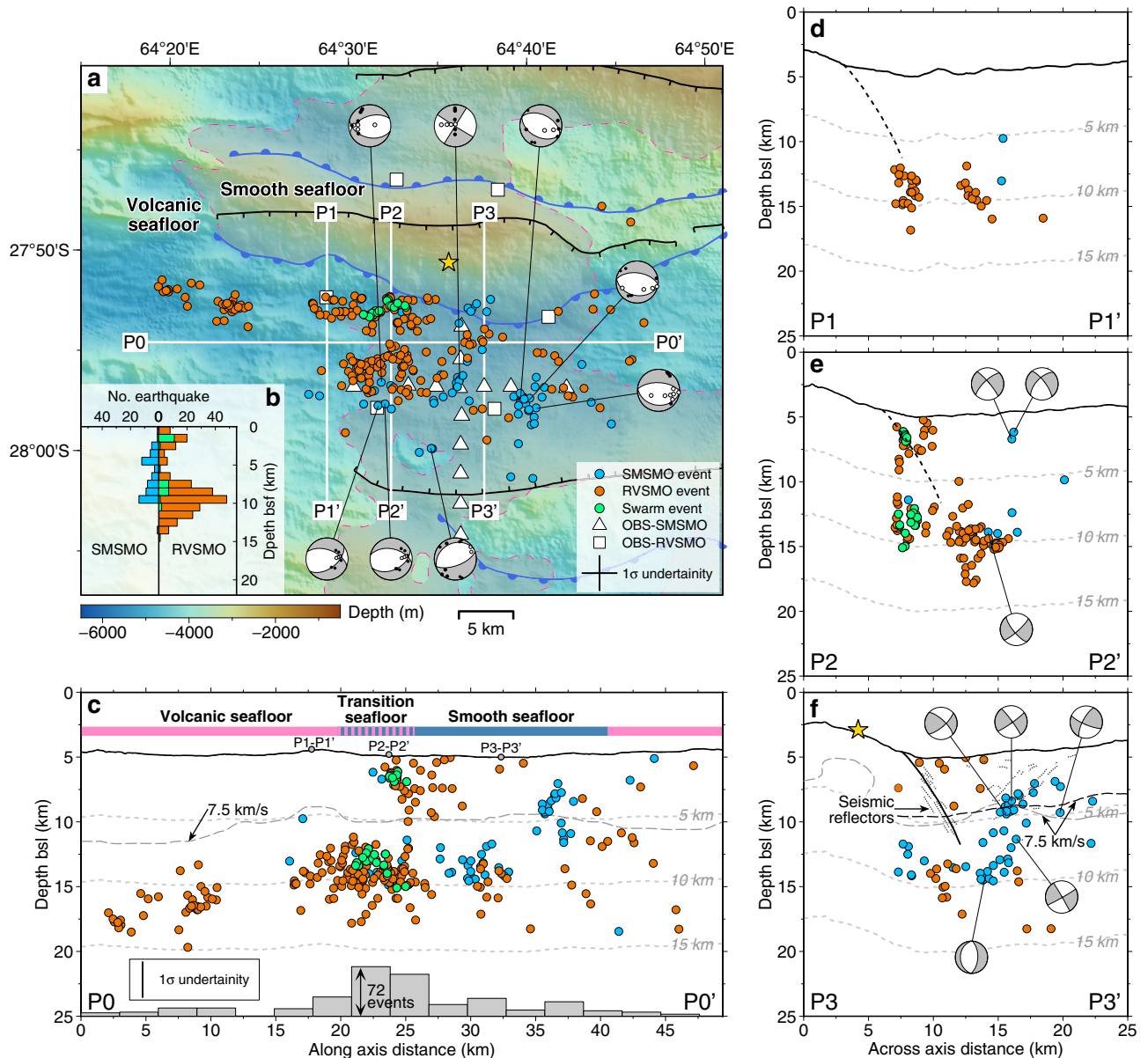


Fig. 2 | Distribution of earthquakes and focal mechanisms. **a** Bathymetric map of the SWIR 64°30'E area showing 307 events of the SMSMO (blue circles) and RVSMO (orange circles) catalogs, the RVSMO seismic swarm (green circles), and 8 determined focal mechanisms. Cross in the legend shows the average absolute horizontal location uncertainty of 3.2 km (1σ). Geological information (see legend for symbols) includes breakaways, emergences, and the boundary between volcanic and smooth seafloor¹. Best-fitting focal mechanisms have clear upward (black dots) and downward (white dots) first motions of P-wave onsets (see the “Methods” section). Depth profiles (P0–P0' to P3–P3') are marked as labeled white lines in **a**. **b** Histograms of earthquake depths below the seafloor for the SMSMO (blue) and RVSMO (orange) catalogs, including the seismic swarm (green). **c** Along-axis depth profile P0–P0' projecting earthquakes within ± 8 km off the profile (VE = 1 and the

same below). The vertical bar shows the average absolute vertical uncertainty of 2.8 km (1σ). The classification of volcanic (pink) and smooth (blue) seafloor is indicated⁴. Gray dashed line is the 7.5 km/s velocity contour³⁹. Labeled gray dashed lines show depths below the seafloor (the same below). **d** and **e** Across-axis depth profiles P1–P1' and P2–P2' projecting earthquakes within ± 3 km off the profiles. Black dashed lines indicate the fault plane adapted from **(f)**. **f** Across-axis depth profile P3–P3' projecting earthquakes within ± 5 km off the profile. Dotted lines represent seismic reflectors, interpreted as DF1 damage zone²³, with the main detachment fault plane tentatively drawn in the center (subseafloor solid black line). Black²³ and gray³⁹ dashed lines are the 7.5 km/s velocity contours. Focal mechanisms are projected to profiles P2–P2' and P3–P3'.

Maximum depth of earthquakes and the axial thermal regime
The thickness of the axial brittle lithosphere, which is commonly interpreted by the maximum depth of earthquakes^{20,25,26}, is predicted to increase as the spreading rate decreases²⁰ and/or as melt supply decreases²⁷. The 64°30'E region of the ultraslow spreading SWIR, being nearly amagmatic, may be regarded as a calibration for the brittle lithosphere thickness of the MOR system. Although our two OBS deployments only recorded a few hundred micro-earthquakes, the maximum depth of earthquake hypocenters is on

the order of 15 km, and this depth is mostly uniform along the ridge axis, across the transition from volcanic to nearly avolcanic smooth seafloor (Fig. 2c). The thickness of the brittle lithosphere is mainly controlled by the thermal regime with its base roughly corresponding to the ~650 °C isotherm^{21,28,29}. This temperature condition is consistent with the minimum depth of 18 km for the 800–1000 °C isotherm at the SWIR 64°30'E, determined from petrological constraints for the high-stress ductile deformation of sheared peridotites^{30,31}.

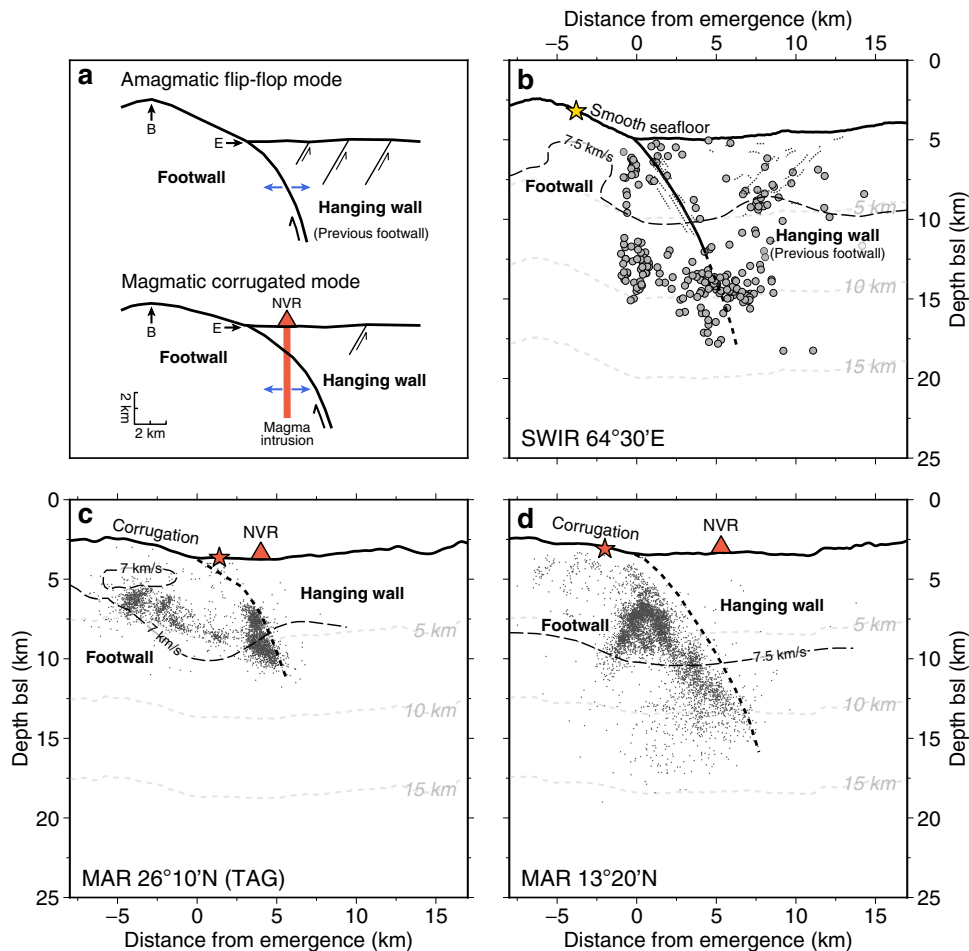


Fig. 3 | Modes of detachment faults and their patterns of seismicity. **a** 2D conceptual sketch of amagmatic flip-flop and magmatic corrugated modes of detachment faults. The flip-flop mode may have more hanging-wall faults to accommodate part of the plate spreading, while this part of plate spreading at the corrugated mode is accommodated by magma intrusions. **b-d** Microseismicity at

the SWIR 64°30'E (this study), and the MAR 26°10'N¹⁵ and 13°20'N^{16,17} (VE = 1). Labeled dashed black lines show velocity contours of 7.5 km/s (SWIR 64°30'E³⁹) and MAR 13°20'N⁵³) and 7 km/s (MAR 26°10'N⁵⁴). Yellow star is the low-temperature Old City hydrothermal vent. Red stars are high-temperature hydrothermal vents. MAR Mid-Atlantic Ridge, NVR neovolcanic ridge, B breakaway, E emergence.

A greater maximum depth of microearthquakes (~20 km) was found at the adjacent magma-poor SWIR 65°10'E³², but these earthquakes were located using a significantly different velocity model constrained from the magmatically robust segment #8 volcano³³ (Supplementary Fig. 2). We also obtain a maximum earthquake depth of ~20 km if we apply their velocity model to our events (see the "Methods" section and Supplementary Fig. 8), although this model is absolutely unsuitable to the nearly amagmatic setting of the SWIR 64°30'E.

Intriguingly, the maximum earthquake depth at the Dragon Horn area (SWIR 49°36'E), which has the same spreading rate but is more magmatic than the SWIR 64°30'E, is also on the order of 15 km^{18,34}. There thus appears to be a disconnection between the maximum earthquake depth and melt supply at ultraslow spreading ridges, putting into question a direct relationship between the thickness of the axial brittle lithosphere and the amount of melt supply to the ridge axis. A recent numerical thermal model provides a possible explanation by considering melt emplacement depth³⁵: at a given spreading rate and melt supply, the thermal regime can be colder if melt is emplaced in the shallow hydrothermally active region. This shallow melt body will be cooled very rapidly, leading to an axial thermal regime beneath the hydrothermal domain that is identical to no melt supply³⁵.

Microseismicity at detachment systems

The seismicity pattern of the active flip-flop detachment fault at the SWIR 64°30'E is characterized by earthquakes aligned with the trace of the detachment fault plane and by coinciding with antithetic normal faults in the detachment hanging wall (Fig. 3b). The detachment-faulting events are similar to those observed at the more magmatic corrugated detachment faults, such as at 26°10'N¹⁵ (TAG), 13°20'N^{16,17}, and 14°50'N (Logatchev) of the Mid-Atlantic Ridge^{15–19} (MAR) and at the SWIR Dragon Horn^{18,34}. However, these detachment faults have very few hanging-wall earthquakes (Fig. 3). We propose that the hanging-wall seismicity may be a signature of the nearly amagmatic flip-flop detachment system, where the plate spreading is accommodated by both detachment and hanging-wall faulting with very few magma intrusions. In contrast to the corrugated mode of detachment faults, magma intrusions are responsible for a considerable part of the plate spreading in the hanging wall, which largely reduces the hanging-wall faulting and seismicity.

In conclusion, our study of two short OBS deployments at an active flip-flop detachment fault system in the nearly amagmatic 64°30'E section of the SWIR reveals a maximum depth of earthquakes of 15 km and hanging-wall seismicity not observed at more magmatic mid-ocean ridge detachment systems. It also suggests that there is a disconnect between the maximum earthquake depth and melt supply at ultraslow spreading ridges.

Methods

Microearthquake experiments

The first experiment, using 14 OBSs in a cross configuration, recorded 8 days of microearthquakes in between airgun shots during the SISMOSMOOTH active seismic survey in October 2014 (R/V *Marion Dufresne*; SMSMO catalog; Fig. 1). The second experiment, using 6 OBSs in a hexagon configuration, continuously recorded 19 days of microearthquakes during the ROVSMOOTH cruise in December 2016 (R/V *Pourquoi Pas?*; RVS MO catalog; Fig. 1). Each OBS recorded three orthogonal ground motions plus pressure signals, with all channels recording at 250 Hz during the SISMOSMOOTH cruise and at 500 Hz during the ROVSMOOTH cruise.

Earthquake detection

The internal clocks of the OBSs were synchronized on deployment and recovery, and a linear drift correction was applied. Earthquake events were network detected by the CONDET program in the SEISAN software³⁶ using the STA/LTA trigger algorithm, and an automatic picking procedure³⁷ was used to pick P and S wave arrival onsets. These events were registered in the SEISAN database, and P- and S-wave arrival onsets were manually refined (Supplementary Fig. 1).

1-D velocity model

The 1-D P-wave velocity model was calculated using the VELEST program³⁸. The initial velocity model was extracted from a seismic refraction experiment across DF1 from the SISMOSMOOTH cruise²³. This model generally agrees with a broader velocity model at the same area³⁹ (Supplementary Fig. 2). Only events with OBS ≥ 6 and GAP $\leq 180^\circ$ were used in the VELEST program. The best-fitting P-wave velocity model was iteratively searched (Supplementary Fig. 2). The final root-mean-square (RMS) is 107 ms. The S-wave velocity (Vs) model is calculated using a best-fitting Vp/Vs ratio of 1.7, based on the Wadati diagram that plots the travel time of P-wave versus travel time differences of P- and S-waves (S-P time; Supplementary Fig. 3).

Earthquake location and relocation

The initial earthquake locations were searched by the NonLinLoc software with the Oct-tree algorithm⁴⁰ and the SWIR 64°30'E velocity model (Supplementary Fig. 2). The maximum-likelihood hypocenter is used to locate each earthquake event, and a three-dimension error ellipsoid (68% confidence) is generated from the posterior density function (PDF) scatter samples⁴⁰. 507 events of SMSMO (122) and RVS MO (385) catalogs were located with four or more stations, and 388 events of SMSMO (88) and RVS MO (300) catalogs are well located with horizontal and depth errors of <5 km and RMS residual of <100 ms (Supplementary Fig. 8a-1-d-1). Station corrections, given by the average travel time residuals at each OBS calculated by the NonLinLoc software in an iterative way, were applied for the P and S phases (Supplementary Fig. 4): the mean absolute station correction is 60 ± 40 ms in both catalogs. P- and S-waves travel time residuals follow the Gaussian distribution with an average RMS misfit of 34 ms (Supplementary Fig. 9). Bootstrap analysis of location errors was applied for four chosen groups of NonLinLoc located events to show the stability of the hypocenter estimates: (1) two swarm events in the RVS MO catalog, (2) two deep events in the RVS MO catalog (beneath smooth and volcanic seafloor), (3) one hanging-wall event in the SMSMO catalog, and (4) two detachment-fault events in both SMSMO and RVS MO catalogs (Supplementary Fig. 10).

We also applied the SWIR 65–66°E velocity model³² (Supplementary Fig. 2), constrained from a more magmatically robust area than our study area^{23,33}, to locate earthquakes recorded in our study area using the NonLinLoc software (Supplementary Fig. 8a-2-d-2). Earthquakes with more distant epicenters to the OBS network tend to have deeper hypocenters to form an inverted V shape of along-axis

hypocenter depth distribution (Supplementary Fig. 8b-2), which is similar to what was proposed at the SWIR 65–66°E³².

NonLinLoc hypocenters with six or more stations, horizontal and depth errors of <5 km, and RMS residual of <100 ms, were relocated using the Double-Difference Hypocenter (HypoDD) algorithm⁴¹. The relocation uses both catalog and cross-correlation (Supplementary Fig. 11a-3-d-3) and runs using the python module HypoDDpy⁴². A time window of 300 ms was applied based on pickings of P and S arrival onsets, and cross-correlated waveforms with a correlation coefficient <0.6 were rejected. Supplementary Fig. 12 shows the differences between the NonLinLoc locations and the HypoDD relocations for 30 randomly selected events. 307 well-constrained absolute hypocenters were relocated with mean relative location errors of 500 m E–W, 400 m N–S, and 500 m in depth.

We also tested catalog only (Supplementary Fig. 11a-1-d-1) and cross-correlation only (Supplementary Figs. 11a-2-d-2) in the HypoDD algorithm, which show more located earthquakes than both catalog and cross-correlation (Supplementary Fig. 11a-3-d-3). Hypocenter location patterns in the three algorithms are relatively stable.

Earthquake magnitude calculation

The definition of local magnitudes (M_L) is given by⁴³

$$M_L = \log(A) + n \log(r) + K r + C, \quad (1)$$

where A (in nm) is the maximum amplitude of horizontal components picked in the Wood–Anderson seismogram⁴⁴, r (in km) is the hypocentral distance, C is a correction for each OBS, and n and K are constants to be calculated, and related to geometrical spreading and attenuation of seismic waves, respectively. The local magnitudes, parameters n and K , and station correction can be solved by a least-squares criterion that produces an optimal solution^{45,46}. For the SMSMO and RVS MO catalogs together, we obtain $n = -2.923$, $K = 5.85 \times 10^{-3}$, and $C = (-3)–(-2)$. Magnitude completeness (M_c) is determined as 1.1 using the b -value stability approach⁴⁷ and resulting in a b -value of 0.9.

First-motion focal mechanism

To calculate best-fitting focal mechanisms, we use two first-motion-based algorithms, HASH⁴⁸ and FOCMEC⁴⁹. Multiple criteria were applied: apparent first-motion polarities of P-wave onsets ≥ 8 , azimuthal gaps $\leq 250^\circ$, the weighted fraction of misfit polarities $<10\%$, RMS of fault plane uncertainty from HASH $\leq 35^\circ$ (95% confidence), and similar reasonable solutions generated by both approaches. Eight acceptable focal mechanisms were found in the SMSMO catalog (Fig. 2). The azimuthal gaps of accepted focal mechanisms are all $>90^\circ$, so their quality grades based on the HASH criteria are all in category E (A is the best constrained). We did not obtain focal mechanisms in the RVS MO deployment due to the lesser number of OBSs.

Data availability

OBS locations, two earthquake catalogs, swarm events, and focal mechanisms in this study are provided in the Supplementary Information. Any remaining raw datasets of this study and additional information on the SISMOSMOOTH⁵⁰ and ROVSMOOTH⁵¹ cruises are available at <https://doi.org/10.17600/14003300> and <https://doi.org/10.17600/16002000>.

Code availability

The software and codes used in this study included: SEISAN software³⁶ (<http://www.seisan.info/>), VELEST program³⁸ (<https://seg.ethz.ch/software/velest.html>), NonLinLoc software⁴⁰ (<http://alomax.free.fr/nlloc/>), Double-Difference Hypocenter (HypoDD) algorithm⁴¹ (Version 2.0; <https://www.ldeo.columbia.edu/~felixw/hypoDD.html>) and its python module HypoDDpy⁴² (<https://doi.org/10.5281/zenodo.18907>),

HASH⁴⁸ and FOCMEC⁴⁹ programs internally in the SEISAN software, and GMT⁵² (Version 6; <https://www.generic-mapping-tools.org/>).

References

1. Cannat, M. et al. On spreading modes and magma supply at slow and ultraslow mid-ocean ridges. *Earth Planet. Sci. Lett.* **519**, 223–233 (2019).
2. Sauter, D. et al. Continuous exhumation of mantle-derived rocks at the Southwest Indian Ridge for 11 million years. *Nat. Geosci.* **6**, 314–320 (2013).
3. Reston, T. Flipping detachments: the kinematics of ultraslow spreading ridges. *Earth Planet. Sci. Lett.* **503**, 144–157 (2018).
4. Cannat, M. et al. Modes of seafloor generation at a melt-poor ultraslow-spreading ridge. *Geology* **34**, 605–608 (2006).
5. Cannat, M. et al. A forest of carbonate-brucite chimneys at the Southwest Indian Ridge: the ultramafic-hosted Old City hydrothermal field. *Goldschmidt Conference Abstract* (2019).
6. Escartín, J. et al. Central role of detachment faults in accretion of slow-spreading oceanic lithosphere. *Nature* **455**, 790–794 (2008).
7. Buck, W. R., Lavier, L. L. & Poliakov, A. N. B. Modes of faulting at mid-ocean ridges. *Nature* **434**, 719–723 (2005).
8. Smith, D. K., Escartín, J., Schouten, H. & Cann, J. R. Fault rotation and core complex formation: Significant processes in seafloor formation at slow-spreading mid-ocean ridges (Mid-Atlantic Ridge, 13°–15°N). *Geochem. Geophys. Geosyst.* **9**, Q03003 (2008).
9. Olive, J. A. & Dublanchet, P. Controls on the magmatic fraction of extension at mid-ocean ridges. *Earth Planet. Sci. Lett.* **549**, 116541 (2020).
10. Cann, J. R. et al. Corrugated slip surfaces formed at ridge-transform intersections on the Mid-Atlantic Ridge. *Nature* **385**, 329–332 (1997).
11. MacLeod, C. J. et al. Life cycle of oceanic core complexes. *Earth Planet. Sci. Lett.* **287**, 333–344 (2009).
12. Escartín, J. et al. Tectonic structure, evolution, and the nature of oceanic core complexes and their detachment fault zones (13°20'N and 13°30'N, Mid Atlantic Ridge). *Geochem. Geophys. Geosyst.* **18**, 1451–1482 (2017).
13. Kong, L. S. L., Solomon, S. C. & Purdy, G. M. Microearthquake characteristics of a mid-ocean ridge along-axis high. *J. Geophys. Res.* **97**, 1659–1685 (1992).
14. Tilmann, F., Flueh, E., Planert, L., Reston, T. & Weinrebe, W. Micro-earthquake seismicity of the Mid-Atlantic Ridge at 5°S: a view of tectonic extension. *J. Geophys. Res. Solid Earth* **109**, B06102 (2004).
15. DeMartin, B. J., Sohn, R. A., Pablo Canales, J. & Humphris, S. E. Kinematics and geometry of active detachment faulting beneath the Trans-Atlantic Geotraverse (TAG) hydrothermal field on the Mid-Atlantic Ridge. *Geology* **35**, 711 (2007).
16. Parnell-Turner, R. et al. Oceanic detachment faults generate compression in extension. *Geology* **45**, 923–926 (2017).
17. Parnell-Turner, R. et al. Seismicity trends and detachment fault structure at 13°N, Mid-Atlantic Ridge. *Geology* **49**, 320–324 (2021).
18. Yu, Z. et al. Lithospheric structure and tectonic processes constrained by microearthquake activity at the central ultraslow-spreading Southwest Indian Ridge (49.2° to 50.8°E). *J. Geophys. Res. Solid Earth* **123**, 6247–6262 (2018).
19. Grevemeyer, I., Reston, T. J. & Moeller, S. Microseismicity of the Mid-Atlantic Ridge at 7°S–8°15'S and at the Logatchev Massif oceanic core complex at 14°40'N–14°50'N. *Geochem. Geophys. Geosyst.* **14**, 3532–3554 (2013).
20. Phipps Morgan, J. & Chen, Y. J. Dependence of ridge-axis morphology on magma supply and spreading rate. *Nature* **364**, 706–708 (1993).
21. McKenzie, D., Jackson, J. & Priestley, K. Thermal structure of oceanic and continental lithosphere. *Earth Planet. Sci. Lett.* **233**, 337–349 (2005).
22. Gutenberg, B. & Richter, C. F. Frequency of earthquakes in California. *Bull. Seismol. Soc. Am.* **34**, 185–188 (1944).
23. Momoh, E., Cannat, M., Watremez, L., Leroy, S. & Singh, S. C. Quasi-3-D seismic reflection imaging and wide-angle velocity structure of nearly amagmatic oceanic Lithosphere at the ultraslow-spreading Southwest Indian Ridge. *J. Geophys. Res. Solid Earth* **122**, 9511–9533 (2017).
24. Momoh, E., Cannat, M. & Leroy, S. Internal structure of the oceanic lithosphere at a melt-starved ultraslow-spreading mid-ocean ridge: insights from 2-D seismic data. *Geochem. Geophys. Geosyst.* **21**, e2019GC008540 (2020).
25. Grevemeyer, I. et al. Constraining the maximum depth of brittle deformation at slow-and ultraslow-spreading ridges using microseismicity. *Geology* **47**, 1069–1073 (2019).
26. Chen, Y. & Morgan, W. J. A nonlinear rheology model for mid-ocean ridge axis topography. *J. Geophys. Res.* **95**, 17583–17604 (1990).
27. Fan, Q., Olive, J. & Cannat, M. Thermo-mechanical state of ultra-slow-spreading ridges with a transient magma supply. *J. Geophys. Res. Solid Earth* **126**, e2020JB020557 (2021).
28. Anderson, D. L. Lithosphere, asthenosphere, and perisphere. *Rev. Geophys.* **33**, 125 (1995).
29. Wang-Pin, C. & Molnar, P. Focal depths of intracontinental and intraplate earthquakes and their implications for the thermal and mechanical properties of the lithosphere. *J. Geophys. Res.* **88**, 4183–4214 (1983).
30. Bickert, M., Cannat, M., Tommasi, A., Jammes, S. & Lavier, L. Strain localization in the root of detachment faults at a melt-starved mid-ocean ridge: a microstructural study of Abyssal Peridotites from the Southwest Indian Ridge. *Geochem. Geophys. Geosyst.* **22**, e2020GC009434 (2021).
31. Bickert, M., Lavier, L. & Cannat, M. How do detachment faults form at ultraslow mid-ocean ridges in a thick axial lithosphere? *Earth Planet. Sci. Lett.* **533**, 116048 (2020).
32. Schlindwein, V. & Schmid, F. Mid-ocean-ridge seismicity reveals extreme types of ocean lithosphere. *Nature* **535**, 276–279 (2016).
33. Minshull, T. A., Muller, M. R. & White, R. S. Crustal structure of the Southwest Indian Ridge at 66°E: Seismic constraints. *Geophys. J. Int.* **166**, 135–147 (2006).
34. Tao, C. et al. Deep high-temperature hydrothermal circulation in a detachment faulting system on the ultra-slow spreading ridge. *Nat. Commun.* **11**, 1–9 (2020).
35. Chen, J., Olive, J. A. & Cannat, M. Thermal regime of slow and ultraslow spreading ridges controlled by melt supply and modes of emplacement. *J. Geophys. Res. Solid Earth* **127**, e2021JB023715 (2022).
36. Havskov, J. & Ottemöller, L. SeisAn earthquake analysis software. *Seismol. Res. Lett.* **70**, 532–534 (1999).
37. Baillard, C., Crawford, W. C., Ballu, V., Hibert, C. & Mangeney, A. An automatic kurtosis-based P-and S-phase picker designed for local seismic networks. *Bull. Seismol. Soc. Am.* **104**, 394–409 (2014).
38. Kissling, E., Ellsworth, W. L., Eberhart-Phillips, D. & Kradolfer, U. Initial reference models in local earthquake tomography. *J. Geophys. Res.* **99**, 19635–19646 (1994).
39. Corbalán, A. et al. Seismic velocity structure along and across the ultraslow-spreading Southwest Indian ridge at 64°30'E showcases flipping detachment faults. *J. Geophys. Res. Solid Earth* **126**, e2021JB022177 (2021).
40. Lomax, A., Virieux, J., Volant, P. & Berge-Thierry, C. Probabilistic Earthquake location in 3D and layered models. In *Advances in Seismic Event Location* (eds Thurber, C. H. & Rabinowitz, N.), chap. 5, 101–134 (Springer, Dordrecht, 2000).

41. Waldhauser, F. & Ellsworth, W. L. A double-difference earthquake location algorithm: method and application to the Northern Hayward Fault, California. *Bull. Seismol. Soc. Am.* **90**, 1353–1368 (2000).
42. Krischer, L. *hypoDDpy: hypoDDpy 1.0* <https://doi.org/10.5281/ZENODO.18907> (2015).
43. Richter, C. F. An instrumental earthquake magnitude scale*. *Bull. Seismol. Soc. Am.* **25**, 1–32 (1935).
44. Anderson, J. A. & Wood, H. O. Description and theory of the torsion seismometer. *Bull. Seismol. Soc. Am.* **15**, 1–72 (1925).
45. Illsley-Kemp, F. et al. Local earthquake magnitude scale and b-value for the Danakil region of northern afar. *Bull. Seismol. Soc. Am.* **107**, 521–531 (2017).
46. Keir, D., Stuart, G. W., Jackson, A. & Ayele, A. Local earthquake magnitude scale and seismicity rate for the Ethiopian rift. *Bull. Seismol. Soc. Am.* **96**, 2221–2230 (2006).
47. Cao, A. & Gao, S. S. Temporal variation of seismic *b*-values beneath northeastern Japan island arc. *Geophys. Res. Lett.* **29**, 48.1–48.3 (2002).
48. Hardebeck, J. L. & Shearer, P. M. A new method for determining first-motion focal mechanisms. *Bull. Seismol. Soc. Am.* **92**, 2264–2276 (2002).
49. Snoker, J., Munsey, J., Teague, A. & Bollinger, G. A program for focal mechanism determination by combined use of polarity and SV-P amplitude ratio data. *Earthq. Notes* **55**, 15 (1984).
50. Leroy, S. & Cannat, M. MD 199/SISMO-SMOOTH cruise, RV Marion Dufresne <https://doi.org/10.17600/14003300> (2014).
51. Cannat, M. ROVSMOOTH cruise, RV Pourquoi pas? <https://doi.org/10.17600/16002000> (2016).
52. Wessel, P. et al. The Generic Mapping Tools Version 6. *Geochem. Geophys. Geosyst.* **20**, 5556–5564 (2019).
53. Simão, N. M. et al. 3-D P-wave velocity structure of oceanic core complexes at 13°N on the Mid-Atlantic Ridge. *Geophys. J. Int.* **221**, 1555–1579 (2020).
54. Zhao, M., Canales, J. P. & Sohn, R. A. Three-dimensional seismic structure of a Mid-Atlantic Ridge segment characterized by active detachment faulting (Trans-Atlantic Geotraverse, 25°55'N–26°20'N). *Geochem. Geophys. Geosyst.* **13**, 2012GC004454 (2012).

Acknowledgements

We thank Sylvie Leroy, chief scientist of the SISMO-SMOOTH cruise, the science parties, and the crews of the RVs *Marion Dufresne* and *Pourquoi Pas* for collecting the data. We also thank Zhiteng Yu, Soumya Bohidar, and Aude Lavayssiére for their help in the data processing. All figures were created using the GMT software⁵². We thank the funding of the ANR project “Ridge-Factory-Slow” (ANR-18-CE010002-01). J.C. was

supported by the China Scholarship Council (201808330437). This is IPGP contribution #4239.

Author contributions

J.C. processed the microseismicity data and wrote the manuscript. W.C.C. supervised data processing, interpretation, and writing. M.C. developed the project, participated in the SISMO-SMOOTH and ROVSMOOTH cruises, led the data collection, and supervised interpretation and writing.

Competing interests

The authors declare no competing interests.

Additional information

Supplementary information The online version contains supplementary material available at <https://doi.org/10.1038/s41467-023-36169-w>.

Correspondence and requests for materials should be addressed to Jie Chen.

Peer review information *Nature Communications* thanks Vera Schlindwein and Robert Sohn for their contribution to the peer review of this work. Peer reviewer reports are available.

Reprints and permissions information is available at <http://www.nature.com/reprints>

Publisher's note Springer Nature remains neutral with regard to jurisdictional claims in published maps and institutional affiliations.

Open Access This article is licensed under a Creative Commons Attribution 4.0 International License, which permits use, sharing, adaptation, distribution and reproduction in any medium or format, as long as you give appropriate credit to the original author(s) and the source, provide a link to the Creative Commons license, and indicate if changes were made. The images or other third party material in this article are included in the article's Creative Commons license, unless indicated otherwise in a credit line to the material. If material is not included in the article's Creative Commons license and your intended use is not permitted by statutory regulation or exceeds the permitted use, you will need to obtain permission directly from the copyright holder. To view a copy of this license, visit <http://creativecommons.org/licenses/by/4.0/>.

© The Author(s) 2023